Available online at www.sciencedirect.com
SCIENCE DIRECT®
International Journal of Heat and Fluid Flow 26 (2005) 119–132
International Journal of HEAT AND FLUID FLOW
www.elsevier.com/locate/ijhff

Normal impingement of a droplet onto a wall film: a numerical investigation

N. Nikolopoulos, A. Theodorakakos, G. Bergeles *

Department of Mechanical Engineering, National Technical University of Athens, Greece 15740 Zografos, Greece

Received 22 April 2002; accepted 7 June 2004
Available online 25 August 2004

Abstract

The paper presents results of a numerical investigation of the impingement process of a droplet normally onto a wall film. The numerical method is based on the finite volume solution of the Navier–Stokes equations, in their axisymmetric formulation, expressing the flow field of the two phases, liquid and gas, coupled by the volume of fluid method (VOF). The latter allows the tracking of the fluid–gas interfaces. The results are compared with available experimental data for integral quantities such as the lamella development in time, whilst the method gives details of the flow fields not hitherto available and which shed light on the droplet interaction with the gas and the mixing mechanisms of the droplet and the wall film during the initial stages of impingement. The latter information is obtained via a 2-VOF model for the prediction of the distribution of mass in the region of lamella during the splash.

Keywords: Deposition; Splashing; Lamella; Liquid film; Volume of fluid method

1. Introduction

The normal impact of a single drop onto a liquid film is a complicated fluid mechanics phenomenon of importance in a variety of engineering areas, such as fuel direct injection into internal combustion engines, spray cooling, spray coating and inkjet printing. The splashing of a droplet normal to a wall film of the same fluid, a phenomenon occurring during the direct fuel injection into the combustion chamber of the internal combustion engines, is governed by non-dimensional parameters including the droplet Weber number (*We*), the Ohnesorge number (*Oh*), Reynolds number (*Re*), Froude number (*Fr*) and the non-dimensional wall film thickness *H*. The droplet impinging normally onto the wall film creates a lamella and a crown whose dimensions vary in time. Fig. 1a and b shows a typical form of a droplet during impingement and some basic global quantities concerning the crown and lamella dimensions; these quantities have been the subject of investigation in the literature. The impingement of the droplet onto the wall film, depending on the initial conditions, can lead to either to droplet deposition or droplet splashing, each of the two cases being followed by other, secondary effects.

A number of numerical studies have been reported for the simulation of the impact of a single droplet on a liquid film. Oguz and Prosperetti (1990) assumed that the flow is axisymmetric, irrotational and thus they introduced the velocity potential to satisfy a Laplace equation; they used the boundary element method for the numerical solution of the equation and a technique to stabilize the calculations due to the presence of surface tension effects; they concluded that a water drop impinging on a water surface may lead to the entrapment of an air bubble at the bottom of the crater. However, Oguz and Prosperetti

* Corresponding author. Address: Laboratory of Aerodynamics–Fluids Section, Department of Mechanical Engineering, National Technical University of Athens, 9 Heroon Polytechniou Avenue, Athens 15773, Greece. Tel.: +30 1 772 10 56; fax: +30 1 772 10 57.
E-mail address: bergeles@fluid.mech.ntua.gr (G. Bergeles).

0142-727X/$ - see front matter
doi:10.1016/j.ijheatfluidflow.2004.06.002

Nomenclature

C_p	non-dimensional pressure ($=\Delta P/\frac{1}{2}\rho_2 U_0^2$)
D_0	initial diameter of droplet
$\vec{f}_\sigma$	volumetric force due to surface tension
Fr	Froude number ($=U_0^2/(gh)$)
h	height of film
H	non-dimensional film height ($=h/D_0$)
K	K number ($=WeOh^{-0.4}$)
$\vec{n}$	vector normal to interface of the two phases
Oh	Ohnesorge number ($=\mu_2/(\sigma\rho_2 D_0)^{0.5}$)
$\vec{q}$	diffusion flux vector of a scalar variable
R	computational radius
R_a	surface roughness
R_{nd}	non-dimensional surface roughness ($=R_a/D_0$)
R_0	radius of initial droplet
Re	Reynolds number ($=\rho_2 D_0 U_0/\mu_2$)
s_{mass}	volumetric mass sources in the mass conservation differential equation
s_u	momentum sources in the momentum conservation differential equation, N/m^3
s_φ	volumetric sources in the conservation differential equation of a scalar variable φ
T	non-dimensional time ($=tU_0/D_0$)
$\vec{T}$	stress tensor
t	time
U_0	initial velocity of droplet
$\vec{u}$	velocity
X	X-axis of computational field
Xdim	non-dimensional X-axis of computational field ($=X/D_0$)
Y	Y-axis of computational field
Ydim	non-dimensional Y-axis of computational field ($=Y/D_0$)
We	Weber number ($=\rho_2 D_0 U_0^2/\sigma$)
We_r	Weber number of the ring ($=\rho_2 D_1 U_1^2/\sigma$)
D_1	diameter of an equilavent droplet of the ring
U_1	velocity of the ring

Greeks

α	volume of fluid (also noted as indicator function)
κ	curvature, m^{-1}
μ	dynamic viscosity
ρ	density
σ	surface tension
φ	scalar variable φ

Subscripts

1	fluid 1 (gas)
2	fluid 2 (liquid)
b	base
l	lamella
r	rim

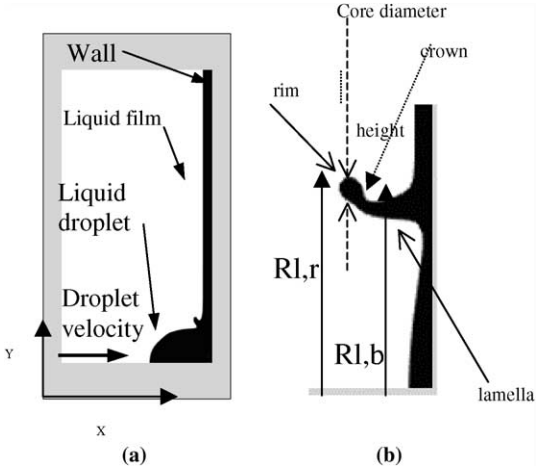

Fig. 1. Definition of impingement characteristics: (a) computational domain; (b) some basic global quantities concerning the crown and lamella dimensions.

(1990) concluded that the range of parameters for which air entrapment occurs is limited and the event has a relatively low possibility of occurrence.

Weiss and Yarin (1999) simulated numerically the axisymmetric impingement of a single drop onto liquid film. Surface tension and gravity were taken into account, whereas viscosity and compressibility were neglected. This allowed the use of the boundary integral method based on the integral equation for the scalar velocity potential. They also observed the entrapment of tiny air bubbles during drop impact on deep liquid films but at low drop velocities only. For impaction on shallow films with relatively high velocities, they observed the development of surface waves on the lamella and formation of the crown. They also observed, under certain conditions, the formation of a liquid jet-like structure which propagated in free space between the impinging drop and the wall liquid film. This jet of liquid, which is formed during impact, reconnects with the wall film trapping a torus-shaped volume of the surrounding gas. They were able to produce analytical relations for the jet tip velocity with drop impact speed; jetting occurs at Weber numbers above a critical value of 40, whilst capillary waves occur at lower than this critical Weber number. The critical Weber number for crown formation is around 100 (for $h/D_0 = 0.125$). At lower Weber numbers, the crown is not formed.

Roisman and Tropea (2002) generalize the potential theory of Yarin and Weiss (1995) to non-axisymmetric cases for high Weber number impacts, and provide expressions for the thickness of the inner and outer liquid films on the wall. The velocity and the thickness of the jet formed on the wall, during the initial stages of the phenomenon, are analytically calculated as are the motion and the crown shape.

Rieber and Frohn (1999) investigated drop impingement by solving, numerically, the Navier–Stokes equations for incompressible fluid in three dimensions. They used the volume of fluid method of Hirt and Nichols (1981) for tracking the liquid gas interfaces. The formulation of the advection terms was fully conservative and it turned out to be essential for a successful simulation of splashing drops. The purpose of the paper was to investigate the instability of the free rim, which leads to the formation of cusps, fingers and secondary droplets. Cusp formation at the free rim was explained by considering the rim as a torus subject to Rayleigh instability. They were able to disintegrate the rim by introducing into the calculation procedure disturbances at the liquid film. Because of this instability, cusps at the free rim of the splashing lamella are formed, which subsequently turn into secondary droplets due to surface tension. From their numerical results, they deduced that the radial extension of lamella is a function of the non-dimensional film thickness and time. Roisman and Tropea (2002) explained the loss of the rim stability and formation of jets by considering small perturbations of the rim centerline.

Yarin and Weiss (1995) describe the evolution of the liquid crown diameter generated by the impact of a drop on a liquid film through the relationship:

$$D(T) = C \cdot D_0 \cdot (T - T_0)^n, \quad n = 0.5, \quad C = \left(\frac{2}{3H}\right)^{0.25} \tag{1}$$

where $D(T)$ is the crown diameter and the exponent n is independent of both drop velocity and film thickness. The constant C is dependent on film thickness but also shows a dependence on the drop impact Weber number. The value of T_0 is also evaluated (by a best fit procedure after n and C are evaluated) and its value ranges between 0 and 1.5.

Further studies of splashing, numerical and experimental, have been made by Bai and Gosman (1995), Stanton and Rutland (1998), and Tropea and Marengo (1998), Cossali et al. (1997, 1999). The present investigation focuses its attention on the interaction of the impinging droplet with the surrounding gas and on the mixing of the drop and wall film during impact, taking into consideration viscous effects. The flow is considered as axisymmetric, therefore normal drop impingement onto the wall layer is considered; the present work considers the effects of viscosity on the flow development and therefore bridges a gap between the axisymmetric integral potential flow approach of Weiss and Yarin (1999) and Oguz and Prosperetti (1990), Morton et al. (2000) and the three-dimensional viscous approach of Rieber and Frohn (1999). The results should be valid for times well beyond the initial stages of impingement up to the appearance of three-dimensional structures (which appear if instabilities occur either in experiment or in the numerical simulation). In this study, numerical simulations are used to provide physical insight into the flow regimes resulting from impingement via detailed velocity and pressure contours.

2. The mathematical problem

The flow induced by a liquid droplet impinging onto a wall liquid film is considered here as two-dimensional axisymmetric, incompressible and laminar; the two-phase flow (phase 2 is the liquid phase, i.e. the droplet and the film, phase 1 is the surrounding gas phase) is represented by the Navier–Stokes equations and the continuity equation with extra terms which take into account the forces due to surface tension and gravity.

For identifying each phase separately a volume fraction, denoted by α, is introduced following the volume of fluid method (VOF) of Hirt and Nichols (1981). In the VOF method the *volume fraction* α is defined as:

$$\alpha = \frac{\text{Volume of fluid 1}}{\textit{Total} \text{ volume of the control volume}} \tag{2}$$

The value of density and viscosity are calculated as a function of α, using linear interpolation between the values of the two phases:

$$\begin{aligned} \rho &= \alpha\rho_1 + (1-\alpha)\rho_2 \\ \mu &= \alpha\mu_1 + (1-\alpha)\mu_2 \end{aligned} \tag{3}$$

where the α-function is equal to:

$$a(x,t) = \begin{cases} 1, & \text{for a point } (x,t) \text{ inside fluid 1} \\ 0, & \text{for a point } (x,t) \text{ inside fluid 2} \\ 0 < \alpha < 1, & \text{for a point } (x,t) \text{ inside the transitional area between the two phases} \end{cases} \tag{4}$$

The momentum equations expressing both phases are written in the form

$$\frac{\partial(\rho\vec{u})}{\partial t} + \nabla \cdot (\rho\vec{u} \otimes \vec{u} - \vec{T}) = \rho\vec{g} + \vec{f}_\sigma \tag{5}$$

where $\vec{T}$ is the stress tensor. The value of f_σ is equal to $f_\sigma = \sigma \cdot \kappa \cdot (\nabla a)$, where σ is the numerical value of the surface tension (for immiscible fluids the value is always positive) and κ is the curvature of the interface region.

For two fluids with indices 1,2 and an interface, the gradient of α gives the vector normal to the interface, which always points away from fluid 2 towards fluid 1:

$$\vec{n} = \nabla a$$

The curvature of the interface Hirt and Nichols (1981) may be expressed in terms of the divergence of the unit normal vector to the interface, as follows:

$$\kappa = -\nabla \cdot \left(\frac{\nabla a}{|\nabla a|} \right) \tag{6}$$

and

$$f_\sigma = -\sigma \cdot \left[\nabla \cdot \left(\frac{\nabla a}{|\nabla a|} \right) \right] (\nabla a) \tag{7}$$

Smoothing of the curvature of the interface by interpolating the gradient values of α on the interface after each time step, across the whole computing field, was found to be necessary. This is achieved by taking into account in a relaxation manner the values of α of the direct neighbors (in both directions X, Y axis) of a cell. Using this technique, the surface of the droplet is smooth, as are also the values of the gradient of α for two neighboring cells.

Following Hirt and Nichols (1981), the location of the interface is calculated on the assumption that the material derivative of the VOF indicator α is zero:

$$\frac{\partial a}{\partial t} + \vec{u} \cdot \nabla a = 0 \tag{8}$$

The continuity equation for both phases in the whole flow field is expressed as:

$$\frac{\partial \rho}{\partial t} + \nabla \rho \vec{u} = 0 \tag{9}$$

The continuity equation, using the conservation of the VOF indicator α, can be written as (Maxwell, 1977):

$$\nabla \cdot \vec{u} = 0 \tag{10}$$

This is the form of the continuity equation (conservation of volume) used in the present simulation.

Using the above equation, the conservative form of the transport equation for α is therefore

$$\frac{\partial a}{\partial t} + \nabla \cdot a\vec{u} = 0 \tag{11}$$

Eqs. (5), (10) and (11) express mathematically the two-phase flow field under consideration.

3. The numerical solution procedure

Transport equations are solved numerically by the finite volume method using a collocated grid arrangement; the discretisation of the convection terms is based on the BSOU method of Papadakis and Bergeles (1995), a second-order, bounded upwind method, whilst the solution procedure for the pressure follows the SIMPLE algorithm of Patankar and Spalding (1972) with the modifications of Rhie and Chow (1983) to avoid pressure–velocity decoupling. Due to the steep gradients of the VOF indicator α which appear particularly in the region of the interfaces, it was found necessary to implement the compressive high-resolution differencing scheme CICSAM of Ubbink and Issa (1999) in the transport equation for α. In contrast with other discretisation schemes, which fail to capture the sharp and smooth interface between the two fluids, it restricts the transitional area of the two fluids within two cells and achieves good resolution of the transitional region. The time derivative was discretized using a second-order differencing scheme (Crank–Nicolson). As a demonstration of the non-diffusive character of the CICSAM scheme, Fig. 2 shows the transport of a square bubble without surface tension effects, moving diagonally, using the hybrid and the CICSAM differencing schemes for the discretisation of the volume fraction α indicator equation. The hybrid scheme, due to its high numerical diffusion, smooths out the surface discontinuity resulting in a round shape, while the CICSAM scheme retains the original shape.

4. Numerical details

The main parameters of the splashing process are film thickness h, droplet diameter D_0 and impact velocity U_0

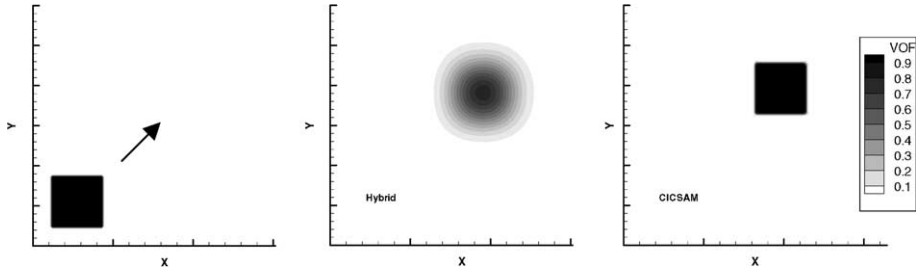

Fig. 2. Diagonal transport of a sharp domain, representing liquid phase using the CICSAM and Hybrid discretisation schemes for the VOF indicator transport equation.

Table 1
The test cases examined

Case	*We*	*Re*	*Oh*	*Fr*	*K*	*H*	Computational domain	Number of grid nodes
A	250	1129	0.0014	366.1	3463	0.116	$2D_0 \times 5D_0$	140×350
B	598	17467	0.0014	868.7	8284	0.116	$2D_0 \times 5D_0$	140×350
B1	598	5523	0.0044	86.87	5226	0.116	$2D_0 \times 5D_0$	140×350
C1	2462	1332	0.037	206	9181	1.71	$3D_0 \times 1.5D_0$	250×125
C2	2540	2492	0.02	206	12092	1.71	$3D_0 \times 1.5D_0$	250×125
D	96.05	4487	0.0022	28.33	1113	3	$7D_0 \times 7D_0$	512×512
E	598	17467	0.0014	100.8	8284	1	$6D_0 \times 6D_0$	500×400
F	598	17467	0.0014	10.08	82848	10	$15D_0 \times 8D_0$	500×267
G	25	2308	0.0022	7.5	295	3	$7D_0 \times 7D_0$	512×512
H	598	1746	0.014	868.7	3296	0.116	$2D_0 \times 5D_0$	140×350

of the single droplet. Other parameters of the problem are the density ρ and viscosity μ of the liquid and gas and the surface tension σ. These variables are grouped in a set of dimensionless parameters, namely the Weber, Reynolds, Ohnesorge and Froude numbers: *We*, *Re*, *Oh* and *Fr*. Two more dimensionless parameters, the film thickness $H = h/D_0$ and the dimensionless time $T = tU_0/D_0$ are introduced.

The flow domain is axisymmetric (about the x axis, which is also the direction in which gravity acts) and the liquid phase (droplet and wall film) is water, whilst the surrounding gas is air. The range of the parameters for which computations have been performed are given in Table 1. For example in cases A, B, and B1 the numerical grid employed consisted of 49000 (140×350) cells and gave the same results with those obtained from a coarser grid of 36000 (120×300). At the start of calculations the droplet is covered by 1855 cells, whilst the wall film is covered by 3150 (9×350).

Cases A, B are identical to those previously studied by Rieber and Frohn (1999) using a 3D approach, whilst cases D and E are numerical experiments to investigate the evolution of ejecta sheet shape at the first stages of impact, and the effect on splashing of the wall film thickness. Cases C1 and C2 have been studied by Thoroddsen (2002), whilst case *H* examines the effect of gas viscosity on the flow development. Weber number is varied by changing the initial velocity of the droplet or, in case B1, the surface tension.

5. Presentation and discussion of the results

5.1. Droplet deposition (case A, Table 1 and Fig. 15a)

Cossali et al. (1997) determined the critical impact Weber number separating the phenomena of deposition and splashing after completing a wide range of experiments. A value of around $We = 200$ was found for the values of *Oh* and *H* considered in cases A and B (Fig. 15). This is confirmed by the present numerical simulation as the case A considered has a *We* number 250, and our predictions indicate marginal splashing. Fig. 3 indicates the vector velocity field at time $T = 0$ (time of contact of the droplet to the film) and subsequent times.

The motion of the droplet towards the liquid wall film induces a gas velocity field, in the form of a vortex ring attached to the droplet, Fig. 3 ($T = 0$); on impingement, a gas jet is formed in the space between the droplet and the liquid surface; the pressure between the droplet and

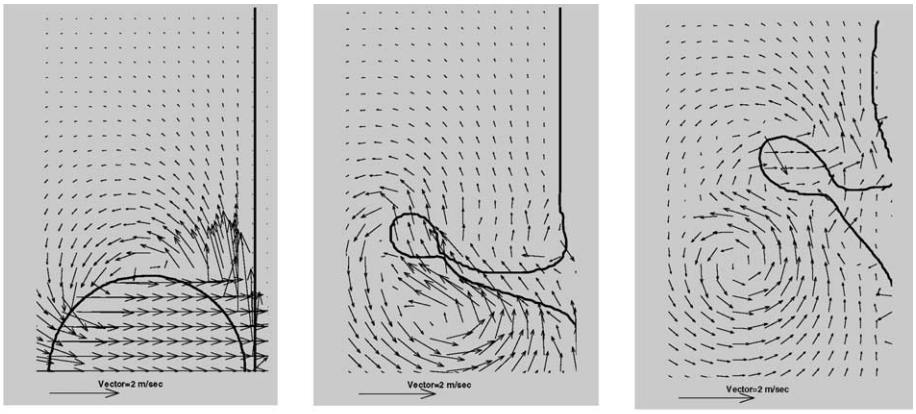

Fig. 3. Velocity field case A (*We* = 250, *Re* = 1129, *Oh* = 0.0014, *H* = 0.116, *Fr* = 366.1).

the surface at the point of impingement increases and deforms the free liquid film surface, the deformation leading to the formation of a liquid jet within the film near the wall propagating into the rest of the wall film, $T = 0.0$. It is of interest to notice the continuity of the velocity field through the gas–liquid interface, as also the well-defined liquid gas interfaces, an indication of the non-diffusive character of the CICSAM discretisation scheme. The liquid wall-jet momentum with the action of the gas vortex ring lifts the liquid off the surface thus leading to the creation of a liquid crown to which a kidney-type vortex ring is attached at the crown rim; the crown, maintaining contact with the droplet and the film, lifts off, increasing both in diameter as also its core diameter. In Fig. 3, $T = 3.03$, the crown rim is on the verge of disintegration, but this does not take place. At time $T = 3.63$ it reaches maximum height (from the undisturbed film surface) and then, while retaining connection with the wall liquid film, starts receding. The droplet impingement also creates capillary waves, which travel on the free liquid surface (Fig. 3, $T = 6.17$), as was also found by Weiss and Yarin (1999). This surface wave starts to appear at about time $T = 4.6$ (after the crown starts receding) having a velocity of about 30% of the initial droplet velocity. At the time of maximum crown height and at the location of drop impingement, a well-formed gas vortex ring occupies the place of the droplet on impingement and the liquid starts rebounding; in subsequent moments the crown recedes and finally mixes with the wall film.

The value of the maximum gas jetting velocity is 430% of the droplet impact velocity, whilst the liquid jetting velocity is 170% of the droplet impact velocity. Values of pressure up to 374% of droplet kinetic energy at the front stagnation point, as is shown in Fig. 4a. Fig. 4b indicates a magnified view of the initial stages of droplet impact on the film, $T = 0.087$, indicating that air bubbles are trapped between the droplet and the film, as has been also found by Oguz and Prosperetti (1990).

The predicted dimensions of the lamella are compared with predictions of the three-dimensional 3D calculations of Rieber and Frohn (1999) as also with the analytic expression of Yarin and Weiss (1995), Eq. (1), Fig. 5. The agreement between the two sets of predictions is very good, suggesting that up to a dimensionless time $T = 3$, which covers the duration of the results presented by Rieber and Frohn (1999) the compressive high-resolution differencing scheme CICSAM of Ubbink and Issa (1999), the flow field is accurately simulated by a 2D axisymmetric approach.

5.2. Droplet splashing (case B, Table 1 and Fig. 15b)

Case B, which is considered here, has a higher Weber number but the same Ohnesorge number and the same dimensionless film thickness as case A. For the present Weber number, the previous investigations from Cossali et al. (1997) indicate that the droplet impingement on the wall film leads to splashing with the creation of secondary droplets due to the crown break-up. This situation is also confirmed by the present numerical simulation.

Fig. 6 shows the velocity vector distribution in the computational domain as a function of time. An air jet and also a liquid jet, like case A, originate from the interaction of the droplet and the film at their contact area. The air jetting velocity takes values up to 423% of the droplet impact velocity, whilst the maximum liquid jetting velocity is 177% of the droplet impact velocity; the pressure distribution along the free liquid surface at the moment of impingement has a similar distribution to that of case A with maximum values up to 374% at the front stagnation point. It is of interest also to note that

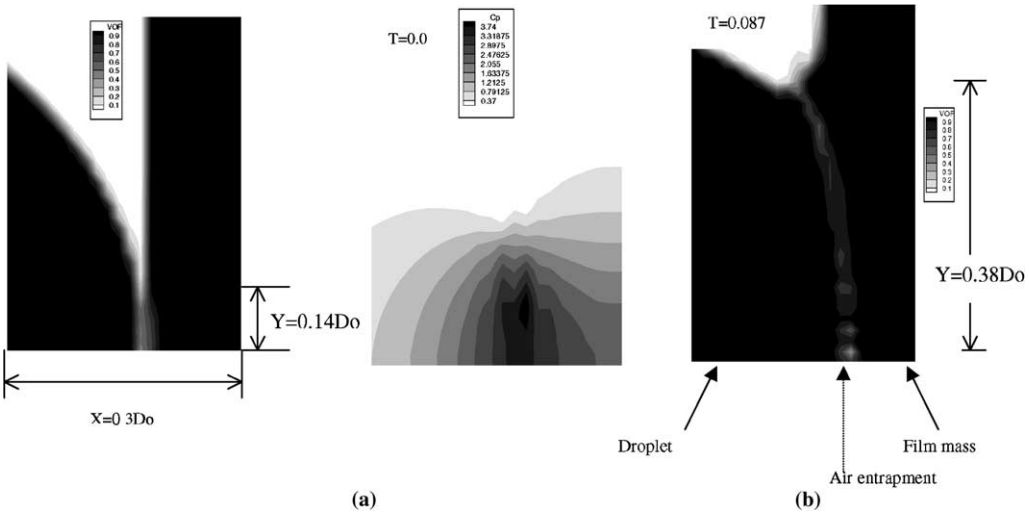

Fig. 4. (a) Pressure contour of the droplet-film interface at $T = 0.0$ and (b) blow-up view of the initial stages of droplet impact on the film at $T = 0.087$.

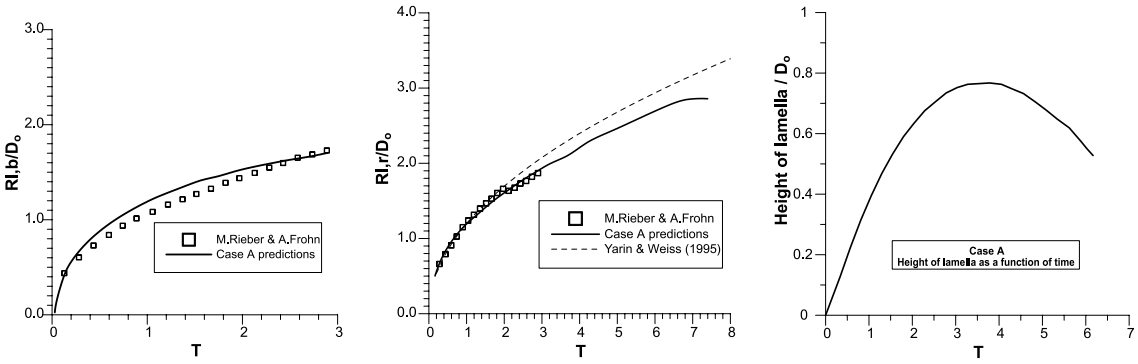

Fig. 5. Comparison of non-dimensional splashing radius and height of lamella for case A ($We = 250$, $Re = 1129$, $Oh = 0.0014$, $H = 0.116$, $Fr = 366.1$).

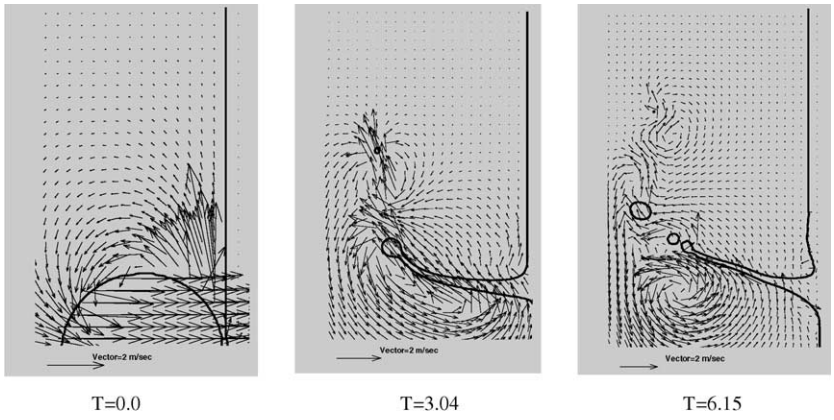

Fig. 6. Velocity field case B ($We = 598$, $Re = 17467$, $Oh = 0.0014$, $H = 0.116$, $Fr = 868.7$).

both the maximum non-dimensional pressure and the air and liquid jetting velocity are about equal in cases A and B, indicating the similarity of the impinging process at the initial stages of droplet impact, independent of Weber number. To support this claim, case B1 has been undertaken maintaining the same *We* number ($We = 598$), but with 10 times lower surface tension; the evolution of the impingement does not change in the early stages of impingement, until about a time $T = 3.65$. The values of the maximum air and liquid jetting velocity agree within 4% to the values of case B and within 7% for the maximum pressure at the front stagnation point. For case B, predictions indicate that the vorticity distribution is stronger in the inner region of the crater than in the corresponding case A. This, in conjunction with the higher momentum that the rim of the crown

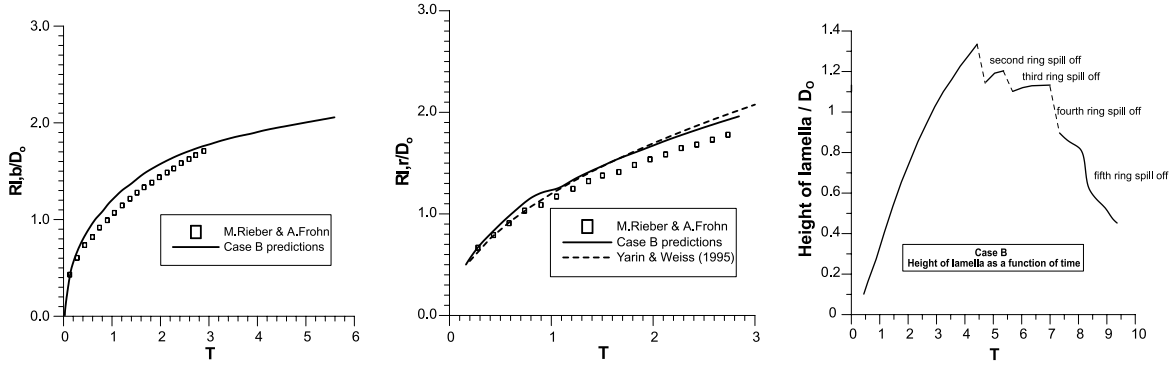

Fig. 7. Comparison of non-dimensional splashing radius and height of lamella for case B ($We = 598$, $Re = 17467$, $Oh = 0.0014$, $H = 0.116$, $Fr = 868.7$).

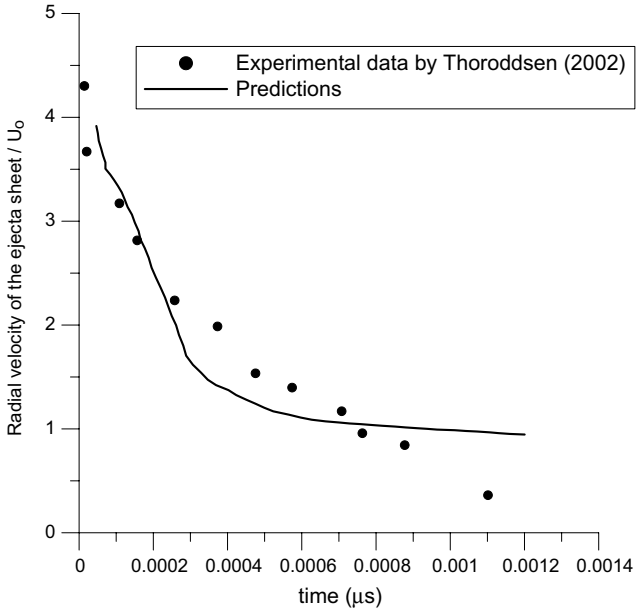

Fig. 8. Radial velocity of the ejecta sheet for $\mu = 29$cP, case C1 ($We = 2462$, $Re = 1332$, $Oh = 0.037$, $H = 1.71$, $Fr = 206$).

possesses, leads to the earlier spill off of secondary, small core diameter, liquid rings and to the break-up of the kidney shaped vortex ring into two isolated air vortex rings (Fig. 6, $T = 3.04$–6.15). The liquid rings, due to their momentum and with the contribution of the air vortex ring, are convected further out from the lamella rim. These rings, either at the time of spill off or later, will become three-dimensional and will break into secondary droplets, a process that the present axisymmetric numerical approach is unable to predict. According to the experimental results of Wachters and Westerling (1966) for a droplet impinging onto a hot surface, the liquid ring which is created breaks up into secondary droplets due to Rayleigh instability if the ring Weber number (We_r) is greater than 80. The ring We_r number for each of the four rings created in case B is 1029, 130, 10.5 and 1.3 respectively. As a result it is expected that at least the two first rings will break up into secondary droplets; however, because the ring mass is small compared with the remaining liquid mass, it is not expected that the spill off of the rings will affect the further evolution of the crown which remains connected to the liquid film.

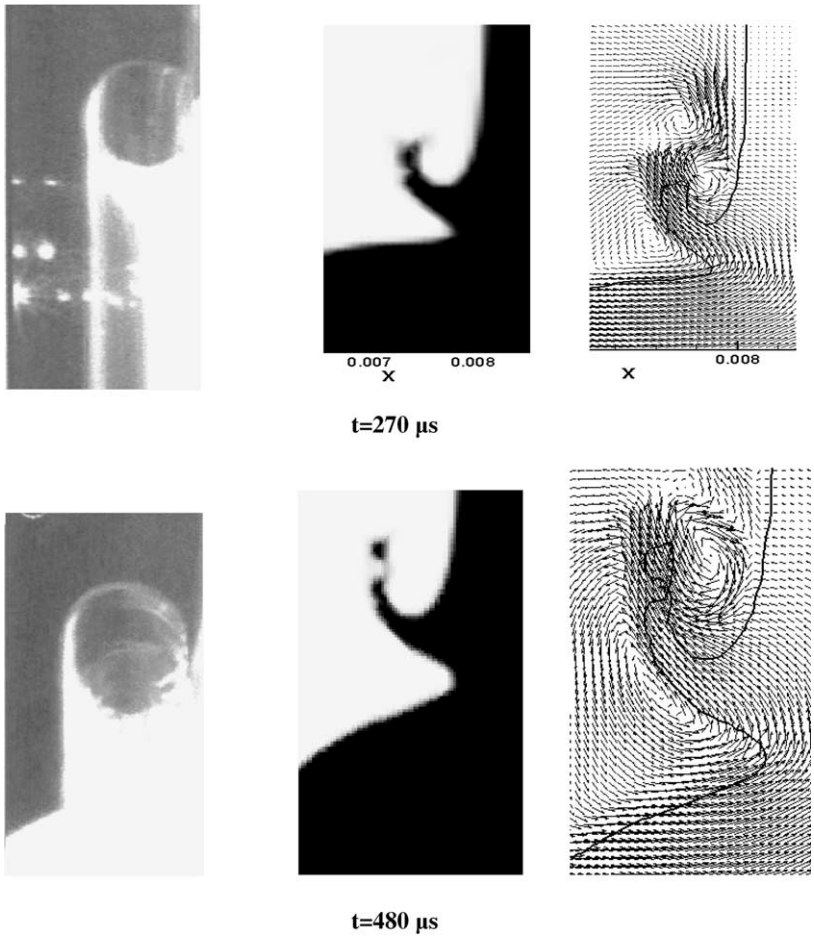

Fig. 9. Evolution of the ejecta sheet for low viscosity, showing the typical bending of the sheet, case C2 (photographs from Thoroddsen, 2002) ($We = 2540$, $Re = 2492$, $Oh = 0.02$, $H = 1.71$, $Fr = 206$).

The predicted dimensions of the lamella are compared with the 3D numerical calculations of Rieber and Frohn (1999) and to the analytic expression of Yarin and Weiss (1995), Eq. (1), Fig. 7. The results indicate that up to a dimensionless time of $T = 3$ for which predictions from Rieber and Frohn (1999) exist, there is a very good agreement with the predictions of the 3D simulation; at times when the crown starts to recede, the present method predicts that the lamella deposits on the film mass, under the action of gravity. In particular Fig. 7c indicates the development of crown height with time. The crown height reaches its maximum value at $T = 4.5$ and then recedes due to gravity and it experiences a sudden decrease due to the spill off of the secondary rings.

5.3. The evolution of ejecta sheet generated in the first stages of the phenomenon, by the impact of the droplet

When a droplet impacts on a liquid film, it ejects a thin horizontal sheet of liquid, emanating from the neck region connecting the two liquid masses. Thoroddsen (2002) studied experimentally the origin, speed and evolution of this ejecta sheet for a range of viscosities. Cases C1 and C2, Table 1, refer to the numerical simulation of the cases studied by Thoroddsen (2002).

Fig. 8 shows comparison of the predicted and measured (as deduced from photographs) radial velocity of the ejecta sheet for the high viscosity case. The maximum radial velocity is 430% of the initial impact velocity. The agreement between the experiment and the simulation is very good. The sheet decelerates rapidly due to the viscous forces induced by the strong radial and azimuthal stretching. Therefore the sheet formation and its development is highly affected by viscosity. Regarding the sheet shape from Fig. 9, it is obvious that the ejecta sheet emanates initially very close to horizontal; however due to the recirculation that it is created in its rim, it bends towards the film surface. The sheet hits the free film surface, while at latter stages the edge is pulled inwards by the combined action of the air vortex and surface tension, impacting onto itself. As a result a torus of entrapped air is formed; obviously the gas phase and its physical properties do affect the further evolution of the phenomenon, in contrast with previous assumptions in numerically simulating this flow by a 2D axially-symmetric potential flow approach.

5.4. Two VOF method

Expanding the VOF method, two more variables VOF1 and VOF2 for the identification of the droplet and the film respectively are introduced. In this way, the methodology is capable of predicting the percentage distribution of the liquid mass in the rings originating from either the droplet liquid or from the wall film

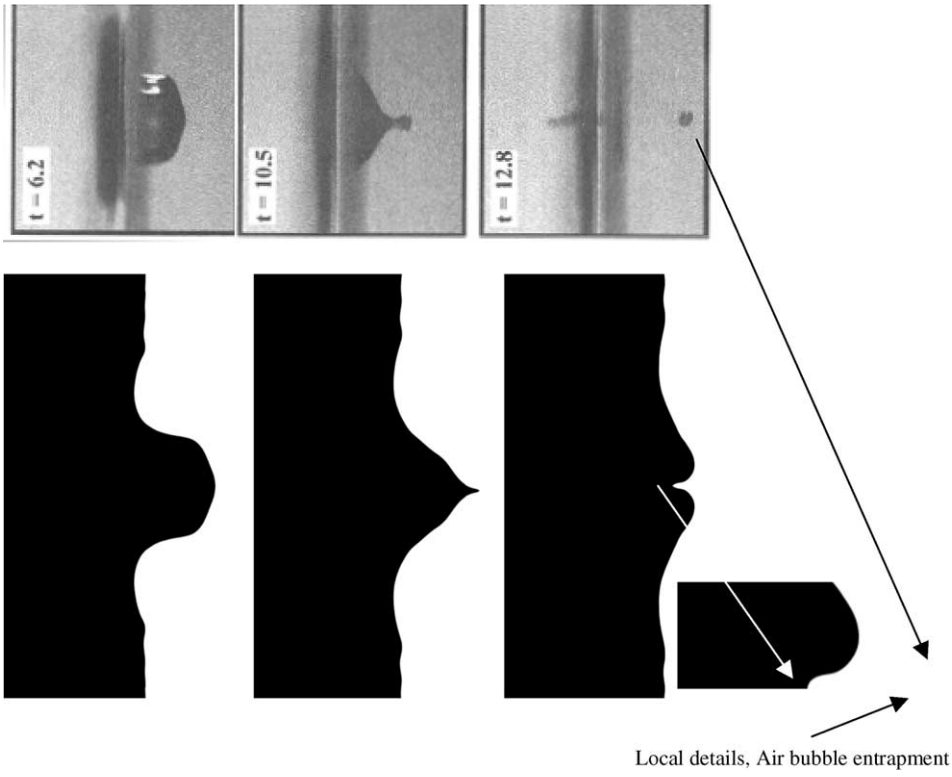

Fig. 10. Comparison of the experimental data and the numerical predictions for case D (reverse colour) (black = air). Photographs from Morton et al. (2000) ($We = 96$, $Re = 4487$, $Oh = 0.0022$, $H = 3$, $Fr = 28.33$).

liquid. In case B, the mass of the lamella consists more from film liquid than from droplet liquid; in particular the first ring has a mass fraction of 72.6% originating from the liquid film, while this fraction increases to 88.1% for the second ring.

5.5. Effect of film thickness

Cases D, E, F (Table 1 and Fig. 16). The impact of a single droplet on a film, with much greater film thickness, compared to case B, was investigated. The accuracy of the simulation is assessed by comparing the numerical results against experimental data obtained by Morton et al. (2000) (case D, Fig. 10). The comparison, Fig. 10, indicates a good qualitative agreement between the predicted and observed free surface behaviour. At the region of impact, a formation like a 'crater' is found. At $T = 10.1$, the receding 'crater' has developed a small cylindrical 'sub-crater'. Afterwards, at $T = 10.5$, the 'mouth' of this 'sub-crater' closes over to entrap an air bubble of $0.2D_0$ in diameter, not captured by the simulations of Morton et al. (2000), but observed in the experiments. The air bubble penetrates into the film ($T = 12.8$), while a thin vertical jet is formed. This jet has an average diameter of 7.5% of the initial droplet diameter.

In cases E and F (see Fig. 16 for sequence of events) the droplet splashes on a film pool, under the same dynamic conditions as case B. The crown of the lamella breaks-up into only one secondary ring of core diameter

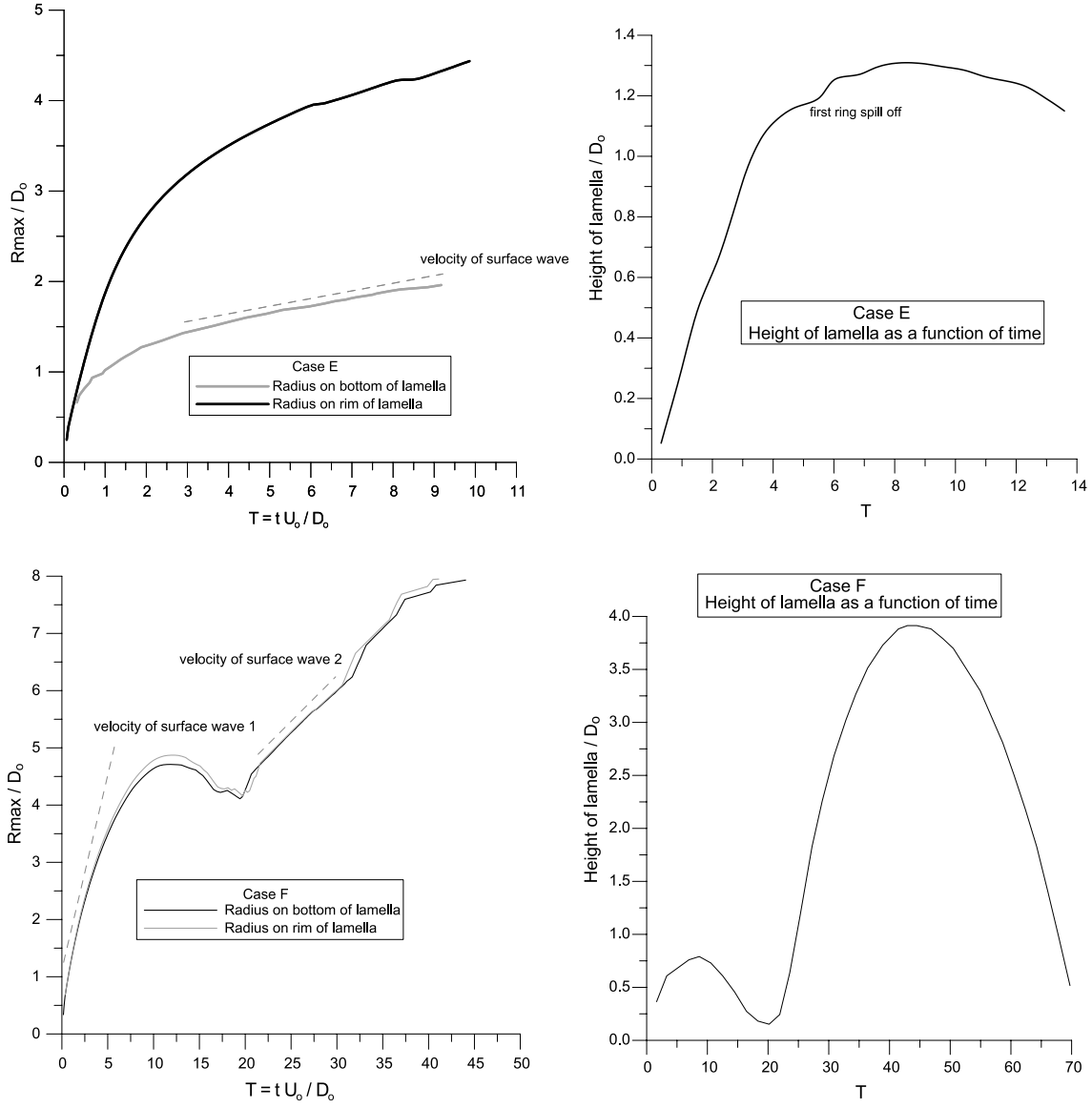

Fig. 11. Comparison of non-dimensional splashing radius and height of lamella for cases E and F. Case E: ($WE = 598$, $Re = 17467$, $Oh = 0.0014$, $H = 1$, $Fr = 100.8$). Case F: ($We = 598$, $Re = 174677$, $Oh = 0.0014$, $H = 10$, $Fr = 10.08$).

7.6% of the initial diameter for case E, similar to the first ring of case B, (Fig. 16a, case E, $T = 2.19$), whilst for case F (Fig. 16b) no spill off occurs. After the lamella reaches its maximum height (Fig. 16a, case E, $T = 8.0$), it starts, under the influence of gravity, to deposit on the remaining mass of film forming a capillary wave, which moves outwards. At the same time, at the bottom and at the inner side of the film, the liquid starts to move inwards. The preceding phenomenon is more pronounced in case F (Fig. 16b, case F, $T \geqslant 6.94$) in which a liquid jet on the symmetry axis is formed, moving upwards. Also, after the first stages of impact, a wave occurs in the liquid film, which is damped with time, due to viscous effects. Fig. 11 shows the dimensions of the lamella as a function of time, for cases E and F. Evidence of the similarity in the impingement processes is the fact that the maximum height of the lamella in case E is the same as that of case B (same Weber number, $H < 3$) and the first ring spills off at about the same time with the same core diameter. In case E, the wave speed is about 11.66% of the initial droplet velocity, whilst in case F a very steep surface wave is formed, as the radius of its rim is close to that at the bottom of the rim. In this case there are two main waves, one in the beginning, which travels at about 61.6% of the droplet speed, and a second one in the later stages of the phenomenon, travelling at 14.1% of the initial droplet velocity.

Case G, Table 1, refers to a lower Weber number compared to case D but for the same fluid (same Ohnesorge numbers) and dimensionless film thickness (case G of Table 1). The numerical results indicate that for this case, due to smaller droplet kinetic energy, air entrapment upon impingement does not take place and also a jet is not formed during the droplet receding phase. Using the 2-VOF model, for case G, it is found that at maximum depth (Fig. 12, $T = 2.5$) the 'crater', caused by impact, is approximately conical and starts to recede; it is evident that the original drop fluid is spread on the internal surface of the cone (Fig. 12, $T = 2.0$ and 2.5), while during the receding phase although the droplet fluid is found mainly on the receding surface, a small amount has also penetrated within the film mass

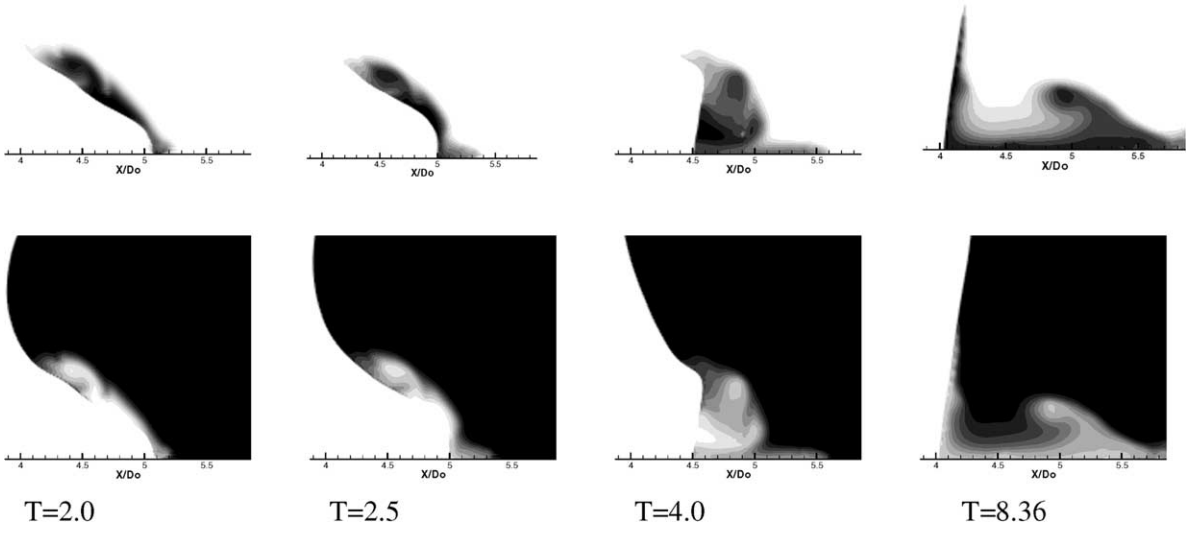

Fig. 12. Evolution of the mixing for case G ($We = 25$, $Re = 2308$, $Oh = 0.0022$, $H = 3$, $Fr = 7.5$), (up) droplet liquid and (down) film liquid.

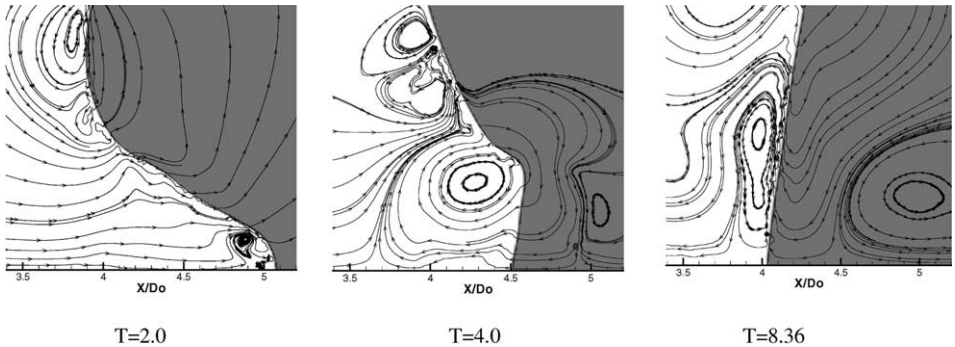

Fig. 13. Streamlines showing vortex rings predicted for case G ($We = 25$, $Re = 2308$, $Oh = 0.0022$, $H = 3$, $Fr = 7.5$); (grey colour = liquid phase).

($T = 4.0$ and 8.36). This can be explained by reference to Fig. 13 which shows streamlines at $T = 4.0$ and 9.0; at $T = 4.0$, the cone is occupied by a large vortex ring which brings film liquid into the cone, contributing to the receding phase. Also a second vortex ring of pure liquid is located below the surface of the crater, which becomes larger at $T = 9.0$. This vortex entraps droplet liquid into the crater of the cone. The predicted two vortex ring structure is also confirmed by experiments (Peck and Sigurdson, 1994; Rein, 1996).

5.6. Effect of viscosity (case H, Table 1)

Weiss and Yarin (1999) investigated case B assuming that the gas viscosity does not play any role on the evolution of splashing phenomenon. This assumption is

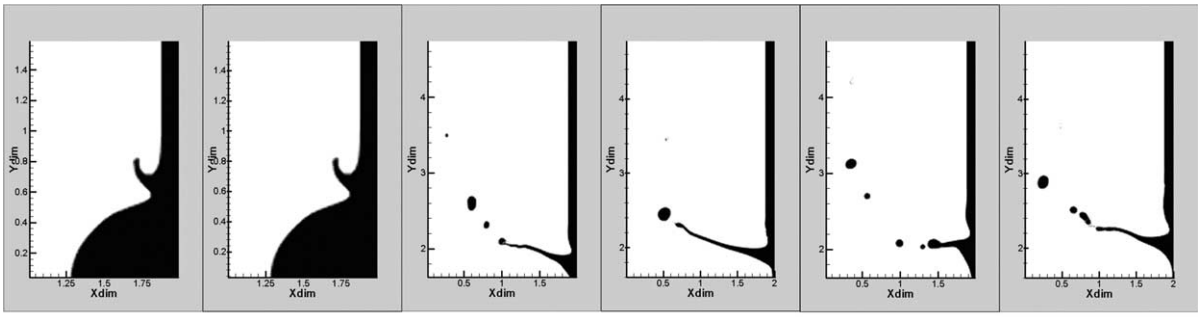

T=0.45 T=5.06 T=7.35

Fig. 14. Effect of viscosity (cases H left–B right). Case B: ($We = 598$, $Re = 17467$, $Oh = 0.0014$, $H = 0.116$, $Fr = 868.7$). Case H: ($We = 598$, $Re = 1746$, $Oh = 0.014$, $H = 0.116$, $Fr = 868.7$).

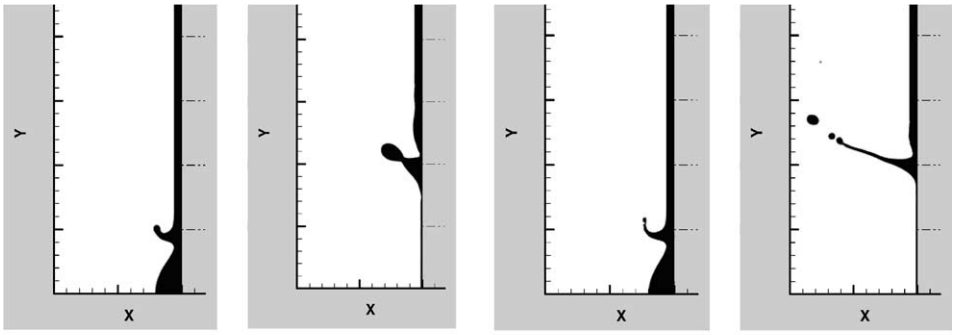

T=0.82 T=6.17 T=0.82 T=6.15

(a) Time sequence of Case A (b) Time sequence of Case B

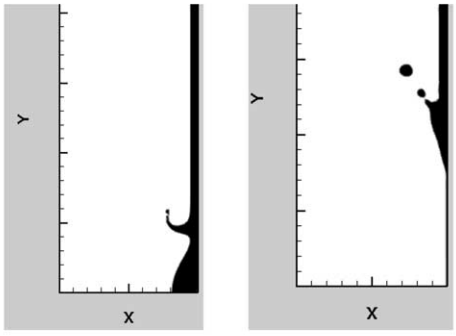

T=0.82 T=6.15

(c) Time sequence of Case B1

Fig. 15. Droplet impinging onto wall film: (a) case A ($We = 250$, $Re = 1129$, $Oh = 0.0014$, $H = 0.116$, $Fr = 366.1$); (b) case B ($We = 598$, $Re = 17467$, $Oh = 0.0014$, $H = 0.116$, $Fr = 868.7$); (c) case B1 ($We = 598$, $Re = 5523$, $Oh = 0.0044$, $H = 0.116$, $Fr = 86.87$).

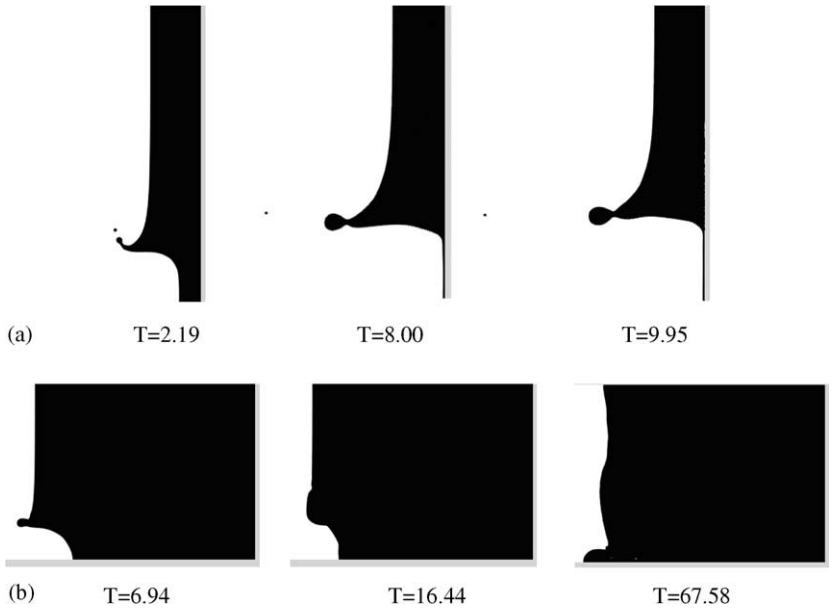

Fig. 16. Droplet impinging onto wall film, with large film thickness, (a) case E (We = 598, Re = 17467, Oh = 0.0014, H = 1, Fr = 100.8); (b) case F (We = 598, Re = 17467, Oh = 0.0014, H = 10, Fr = 10.08).

confirmed by the present results for the initial stages of splashing, indicating that for the initial stages of flow development ($T < 3$) viscosity is not important and can be neglected in the calculations.

The viscosity of gas is influential, however, in the later stages of splash evolution, when secondary rings are on the verge of spill off due to the shear forces that are developed in the rim of lamella. In order to identify the role of viscosity, cases B and H are compared. The conditions of each case are shown in Table 1. In case H the value of viscosity is 10 times that of the corresponding value of case B. From Fig. 14 it is obvious that up to a dimensionless time $T = 3.0$ viscosity does not play any significant role in the evolution of splashing. After that time, the different magnitude of shear forces around the rim of lamella lead to the spill off (and subsequent break up) of more secondary rings in case H than in case B, as is shown in Fig. 14 for dimensionless times of $T = 5.06$ and 7.35, unless 3D instabilities develop before ring spill off.

6. Conclusions

The flow development arising from the normal impingement of a droplet onto a wall film was numerically studied using a finite volume methodology with the volume of fluid (VOF) technique. A higher order discretisation scheme was found imperative for the numerical solution of the transport equation for the VOF indicator in order to accurately track the droplet-wall film interface. The axisymmetric numerical simulation which was adopted proves to be accurate up to the time of formation of the liquid crown; later, at spill off, 3D effects may appear on the lamella rim. The results indicate that viscosity does not play a significant role in the early stages of droplet impingement, but it does however affect the evolution of the ejecta sheet generated upon droplet impact on the film; also, the spill off of secondary rings, their number and their motion, depends on viscous effects. Splashing development, up to the spill off of rings, shows similarity for the Weber numbers studied, but the film thickness is influential for the latter stages of flow development. The employment of the two VOF indicators for the droplet and wall film allows the conclusion that most of the spill off rings contain liquid from the wall film for the cases of small film thickness. The VOF method was capable of predicting the details of the fine scales, of the flow field, like air bubble entrapment, capillary waves, and air and liquid jetting.

Acknowledgment

The financial support of the EU under contract no. ENK6-2000-00051 is acknowledged.

References

Bai, C., Gosman, A.D., 1995. Development of methodology for spray impingement simulation. Society Automot. Engng. 950283.

Cossali, G.E., Goghe, A., Marengo, M., 1997. The impact of a single drop on a wetted solid surface. Exp. Fluids 22, 463–472.

Cossali, G.E., Brunello, G., Goghe, A., Marengo, M., 1999. Impact of a single drop on a liquid film: experimental analysis and comparison

with empirical models. In: Italian Congress of Thermofluid Dynamics UIT, Ferrara, 30 June–2 July.
Hirt, C.W., Nichols, B.D., 1981. Volume of fluid (VOF) method for the dynamics of free boundaries. J. Comput. Phys. 39, 201–225.
Maxwell, T.T., 1977. Numerical Modelling of Free Surface Flows. Phd Thesis, University of London.
Morton, D., Rudman, M., Jong-Leng, L., 2000. An investigation of the flow regimes resulting from splashing drops. Phys. Fluids 12 (4), 747–763.
Oguz, N.H., Prosperetti, A., 1990. Bubble entrainment by the impact of drops on liquid surfaces. J. Fluid. Mech. 219, 143–179.
Papadakis, G., Bergeles, G., 1995. A locally modified second order upwind scheme for convection terms discretisation. Int. J. Num. Meth. Heat Fluid Flow 5, 49–62.
Patankar, S.V., Spalding, D.B., 1972. A calculation procedure for heat, mass and momentum transfer in three dimensional parabolic flows. Int. J. Heat Mass Transfer 15, 1787–1806.
Peck, B., Sigurdson, L., 1994. The three dimensional vortex structure of an impacting water drop. Phys. Fluids 6, 564.
Rein, M., 1996. The transitional regime between coalescing and splashing drops. J. Fluid. Mech. 306, 145.
Rhie, C.M., Chow, W.L., 1983. A numerical study of the turbulent flow past an isolated airfoil with trailing edge separation. AIAA J. 21, 1525–1532.
Rieber, M., Frohn, A., 1999. A numerical study on the mechanism of splashing. Int. J. Heat Fluid Flow 20, 455–461.
Roisman, I.V., Tropea, C., 2002. Impact of a drop onto a wetted wall: description of crown formation and propagation. J. Fluid Mech. 402, 373–397.
Stanton, D.W., Rutland, C.J., 1998. Multi-dimensional modeling of thin liquid films and spray-wall interactions resulting from impinging sprays. Int. J. Heat Mass Transfer 41, 3037–3054.
Thoroddsen, S.T., 2002. The ejecta sheet generated by the impact of a drop. J. Fluid Mech. 451, 373–381.
Tropea, C., Marengo, M., 1998. The impact of drops on walls and films. In: Third International Conference on Multiphase Flow, ICMF '98, Lyon, France, June 8–12.
Ubbink, O., Issa, R.I., 1999. A method for capturing sharp fluid interfaces on arbitrary meshes. J. Comput. Phys. 153 (1), 26–50.
Wachters, L.H., Westerling, N.A.J., 1966. The heat transfer from a hot wall to impinging water drops in the spheroidal state. Chem. Eng. Sci. 21, 1047–1056.
Weiss, A.D., Yarin, L.A., 1999. Single drop impact onto liquid films: neck distortion, jetting, tiny bubble entrainment, and crown formation. J. Fluid. Mech. 385, 229–254.
Yarin, L.A., Weiss, A.D., 1995. Impact of drops on solid surfaces: self-similar capillary waves, and splashing as a new type of kinematic discontinuity. J. Fluid. Mech. 283, 141–173.